Advanced Composite Materials
Publication details, including instructions for authors and subscription information:
http://www.tandfonline.com/loi/tacm20

Fracture Resistance of Carbon/Epoxy Composite Laminates under Mixed-Mode II and III Failure and Its Dependence on Fracture Morphology

Atsushi Kondo [a] , Yuta Sato [b] , Hiroshi Suemasu [c] & Yuichiro Aoki [d]

[a] Graduate School, Sophia University, 7-1 Kioi-cho, Chiyoda-ku, Tokyo 102-8554, Japan;, Email: akondo@sophia.ac.jp

[b] Graduate School, Sophia University, 7-1 Kioi-cho, Chiyoda-ku, Tokyo 102-8554, Japan

[c] Department of Science and Technology, Sophia University, 7-1 Kioi-cho, Chiyoda-ku, Tokyo 102-8554, Japan

[d] Japan Aerospace Exploration Agency, 6-13-1 Osawa, Mitaka-shi, Tokyo 181-0015, Japan

Version of record first published: 02 Apr 2012.

To cite this article: Atsushi Kondo , Yuta Sato , Hiroshi Suemasu & Yuichiro Aoki (2011): Fracture Resistance of Carbon/Epoxy Composite Laminates under Mixed-Mode II and III Failure and Its Dependence on Fracture Morphology, Advanced Composite Materials, 20:5, 405-418

To link to this article: http://dx.doi.org/10.1163/092430411X568197

VSP

Advanced Composite Materials 20 (2011) 405–418

ADVANCED COMPOSITE MATERIALS
brill.nl/acm

Fracture Resistance of Carbon/Epoxy Composite Laminates under Mixed-Mode II and III Failure and Its Dependence on Fracture Morphology

Atsushi Kondo [a,*], **Yuta Sato** [a], **Hiroshi Suemasu** [b] **and Yuichiro Aoki** [c]

[a] Graduate School, Sophia University, 7-1 Kioi-cho, Chiyoda-ku, Tokyo 102-8554, Japan
[b] Department of Science and Technology, Sophia University, 7-1 Kioi-cho, Chiyoda-ku, Tokyo 102-8554, Japan
[c] Japan Aerospace Exploration Agency, 6-13-1 Osawa, Mitaka-shi, Tokyo 181-0015, Japan

Received 19 August 2010; accepted 30 January 2011

Abstract

The fracture resistance of composite laminates under mixed-mode II and III stable damage propagation conditions and its dependence on the fracture morphology were experimentally studied. Cross-ply carbon/epoxy composite specimens were tested by the double notched split cantilever beam (DNSCB) test method. Complex damage consisting of delaminations and shear-induced matrix cracks grew in the middle of the specimen. The delaminations propagated outside the complex damage region. The energy release rate was decomposed to transverse and parallel components to the fiber, G_{ST} and G_{SL}. The component G_{ST} was almost zero at the simple delamination edges and very high in the region of complex damage. The fracture resistances in the regions of complex damage and simple delaminations were numerically evaluated. The fracture resistance was 1.5–2 times higher in the complex damage region than in the simple delamination region.

Keywords

Mixed mode, fracture toughness, delamination, experiment, finite element analysis

1. Introduction

Because of the inherent weakness of the interface of laminated composites, characterization of interlaminar fracture is crucial in the analysis of the failure of these materials. As the interlaminar fracture of laminated composites generally occurs under mixed-mode I, II and III conditions, the fracture behavior under all three individual and/or mixed modes should be characterized.

* To whom correspondence should be addressed. E-mail: akondo@sophia.ac.jp

DOI:10.1163/092430411X568197

The propagation conditions of interlaminar fracture are usually discussed in terms of interlaminar fracture toughness based on linear fracture mechanics. There have been numerous studies on the evaluation of interlaminar fracture toughness. Mode I and mode II fracture toughnesses were widely evaluated for various material systems [1–6]. Mode II fracture toughness was generally reported to be greater than mode I fracture toughness. Studies on mixed-mode I and II fracture toughness also reported that fracture toughness increased with the increase of the ratio of the mode II component [7–9]. Several researchers studied fracture morphology under mixed-mode I and II failure [10–12]. Shear cusps, also called shear hackles, were formed by microcracking at the interply resin region ahead of the crack tip when the mode II component was present. This occurrence explained the difference between mode I and mode II fracture toughness. A number of studies reported that mode III fracture toughness was significantly greater than the fracture toughness of the mode II component [13–17]. It was also pointed out that many inclined matrix cracks appeared along the fibers in the layers adjacent to the delaminated plane under mode III failure, and these cracks possibly affected the fracture toughness [18, 19]. If this change in fracture morphology is the reason for the difference between mode II and mode III fracture toughnesses, its effect should also appear under mixed-mode II and III failure. Recently, evaluation of mixed-mode II and III fracture toughness was made possible by the development of two test methods [20, 21]. These evaluations, however, reported little dependence of the fracture toughness on the mixed-mode ratio and did not mention the fracture morphology. The evaluated fracture toughness might not include the specific effect of shear-induced matrix cracks because the test methods were intended to measure the initiation toughness. As the shear-induced matrix cracks are primarily produced during delamination propagation [19], a test method to realize stable crack growth is necessary to evaluate the fracture resistance and the effect of shear-induced matrix cracks.

The authors proposed the double notched split cantilever beam (DNSCB) test method [22], which enabled stable delamination propagation under the mixed-mode II and III condition. They evaluated the mixed-mode II and III fracture resistance of CFRP laminates under stable delamination propagation by using the DNSCB test method [23]. They found a clear dependence of the fracture resistance not on the mixed-mode ratio but on the fracture morphology.

In this paper, the condition of the fracture morphology change is studied and the dependence of the fracture resistance on the fracture morphology is evaluated.

2. Experimental

2.1. Test Method

The DNSCB test method was used to study the fracture behavior of composite laminates during stable propagation of delaminations under the mixed-mode II and III condition. The beam-like specimen shown in Fig. 1 is used for this test. Two symmetrically located starter cracks are introduced to avoid twisting deformation. By

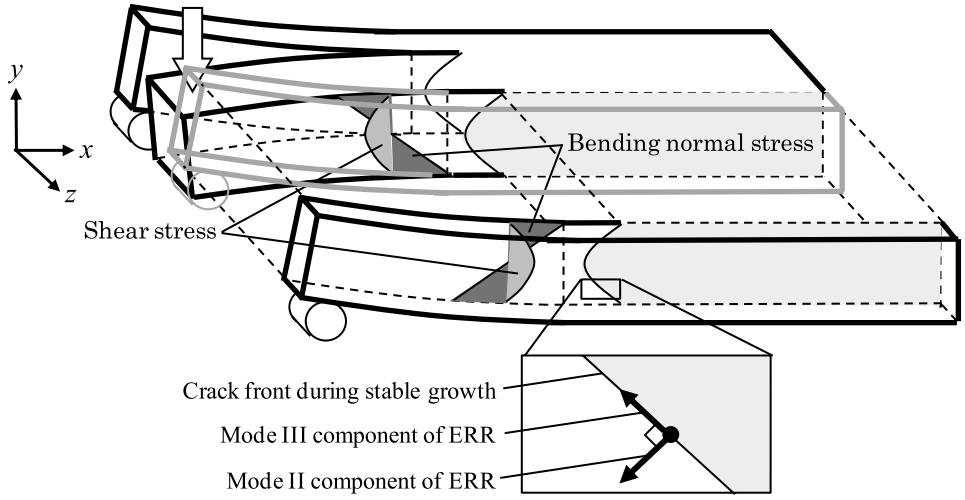

Figure 1. Concept of DNSCB test method.

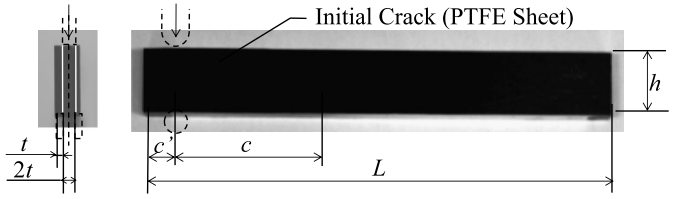

Figure 2. Specimen used in the test.

bending the outer and inner portions of the specimen in opposite directions, the combination of bending normal stress and shear stress in the beam causes general mixed-mode shear fracture at the crack front. This test method has two notable features: stable crack propagation and a varying mixed-mode ratio along the curved crack front. During stable crack propagation, the energy release rates along the crack front are recognized as the fracture resistance because the critical condition is satisfied along the crack front. Distributions of the energy release rate components were numerically calculated with the virtual crack closure technique (VCCT).

2.2. Test Specimens and Apparatus

The specimens, shown in Fig. 2, were made of prepreg TR380G-250SM (Mitsubishi Rayon Inc.). The stacking sequence of each specimen was $[[0/90]_{2s}//[0/90]_{2s}]_s$. Two starter cracks were made at the interfaces of the two 0° layers by inserting PTFE films of 20 μm thickness. Four combinations of dimensions were adopted to check whether the evaluated fracture resistances depend on the specimen dimensions. The specimen length L and the thickness of the cracked portion t were 150 and 1.8 mm, respectively, for all of the specimens. The height h of the specimens was 10 and 20 mm, and the length c of the starter cracks was 40 and

Table 1.
Material properties of unidirectional material

E_L (GPa)	E_T (GPa)	ν_{LT}	ν_{TT}	G_{LT} (GPa)	G_{TT} (GPa)	G_{Ic} (J/m^2)	G_{IIc} (J/m^2)
122	8.16	0.34	0.5	4.13	2.70	378	767

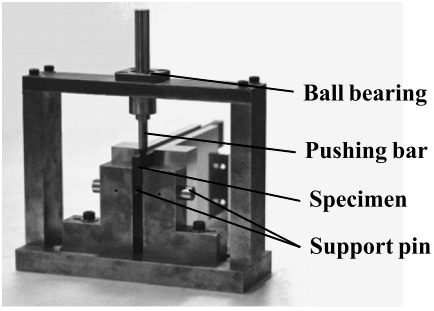

Figure 3. Test apparatus.

80 mm. The specimen types were named according to these dimensions. For example, the name of the specimen with $h = 20$ mm and $c = 80$ mm was h20c80. Three tests were conducted for each type of specimen. The mechanical properties of the unidirectional specimens are shown in Table 1. The elastic constants were determined based on tensile tests. The mode I and mode II fracture toughnesses of the interface of the two 0° layers were evaluated with the double-cantilever beam (DCB) and end-notched flexure (ENF) tests, respectively.

Figure 3 shows the apparatus used in the test. A specimen was placed between two blocks so that portions of the specimen did not tilt in the out-of-plane direction, and the bottom surfaces of the outer portions of the specimen were supported by round pins. The positions of the round pins were adjusted to the thickness of the outer portions of the specimen. The top surface of the center portion of the specimen was loaded by a vertical bar with a round tip. The vertical bar was supported by ball bearings so that the bar remained upright. The apparatus was set under the crosshead of a static testing machine (Auto-Graph AG-10TB, Shimadzu Inc.) and the crosshead speed was set at 0.25 mm/min. The crack front shapes were observed with an ultrasonic C-Scan system (Mi-scope hyper, Hitachi Inc.).

2.3. Test Results and Discussion

Figure 4 shows the relations between the applied load and the displacement of the crosshead obtained from the test of the h20c80 specimen. The load increased linearly with the increase of the applied displacement. The increase of the compliance was smooth, as in the DCB tests, and suggested that the delaminations propagated stably during the test. After several millimeters of the delamination propagation, the test was suspended and the shapes of the crack fronts were observed with the

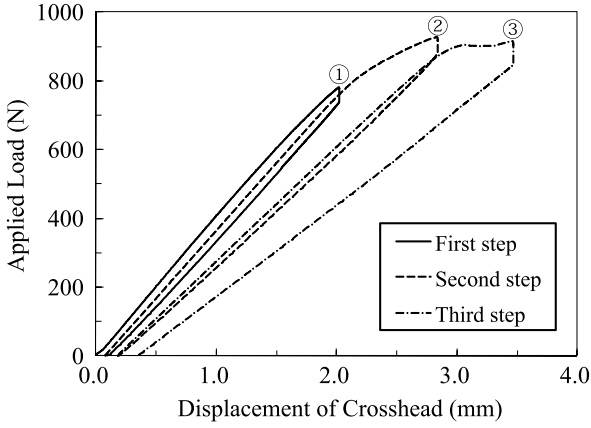

Figure 4. Load–displacement relations.

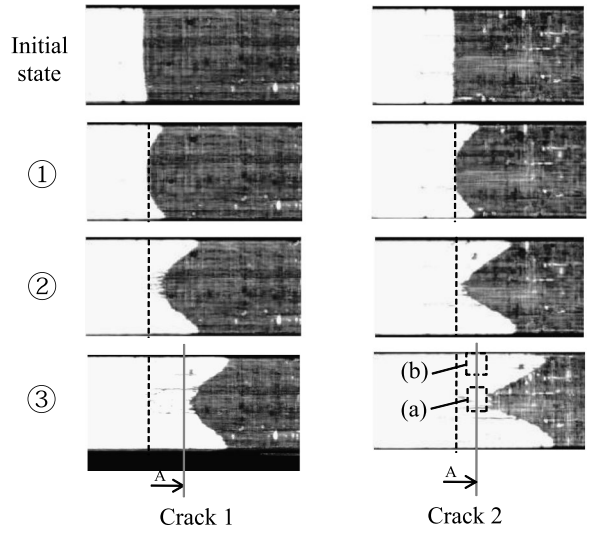

Figure 5. Ultrasonic C-Scan images of crack fronts.

ultrasonic C-Scan. This procedure was repeated several times. At each step the load–displacement relation was measured, and the change of the crack front shape was captured. The shapes of the two crack fronts are shown in Fig. 5. The numbers in Fig. 5 correspond to those in Fig. 4. The white and black areas indicate the delaminated and intact areas, respectively.

In the first test, the delamination started to propagate from the edge of the crack front. In the second test, the delamination spread toward the centerline of the specimen. The delamination near the edge propagated more than that in the middle of the crack front. Finally, smooth curved crack fronts were created. The shapes of the crack fronts were almost symmetric. The delamination grew stably while keep-

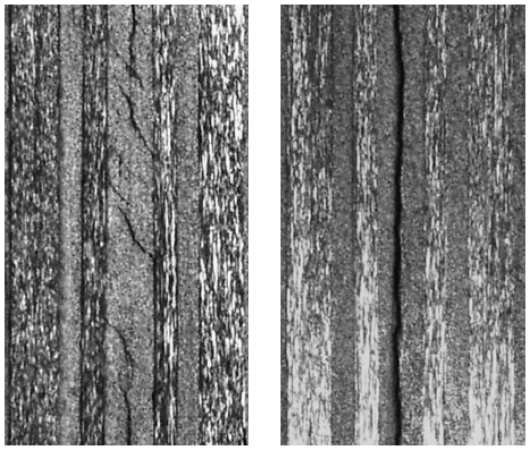

(a) (b)

Figure 6. Micrographs of cross-sections of damage regions. (a) Region of complex damage. (b) Region of simple delamination.

ing similar crack front shapes. The propagation lengths of the two cracks were not exactly the same due to the probabilistic nature of the fracture behavior.

Scattered signals existed near the centerline of the specimen in front of the cracks in the C-Scan images taken after phases 2 and 3. The specimen was cut at position A, shown in Fig. 5, and its cross-section was observed with an optical microscope. Micrographs of regions (a) and (b) in Fig. 5 are shown in Fig. 6. Distributed matrix cracks were observed in the 0° layers adjacent to the delamination plane in region (a). This region corresponds to the area of the scattered signals in the C-Scan image. In region (b), no matrix cracks were observed. We call regions (a) and (b) the complex damage region and the simple delamination region, respectively.

As shown in Fig. 7, shear stress τ_{yz} was dominant in the complex damage region and shear stress τ_{xz} was dominant in the simple delamination region. Since shear stress τ_{yz} caused tensile stress in the plane normal to the fiber, the distributed matrix cracks occurred in the complex damage region. Shear stress τ_{xz} caused no tensile stress at all in the plane normal to the fiber and, therefore, the delamination grew in the original interface without the accompanying matrix cracks.

3. Evaluation of Fracture Resistance

3.1. Energy Release Rate Distribution

The energy released during propagation of a unit area of damage was numerically calculated to evaluate the fracture resistances in both the complex damage and the simple delamination regions. Finite element analyses were conducted using the commercially available code Abaqus 6.7. In the simple delamination region, the fracture resistance can be considered as a material constant, i.e., the interlaminar fracture toughness, but in the complex damage region, the fracture resistance is not

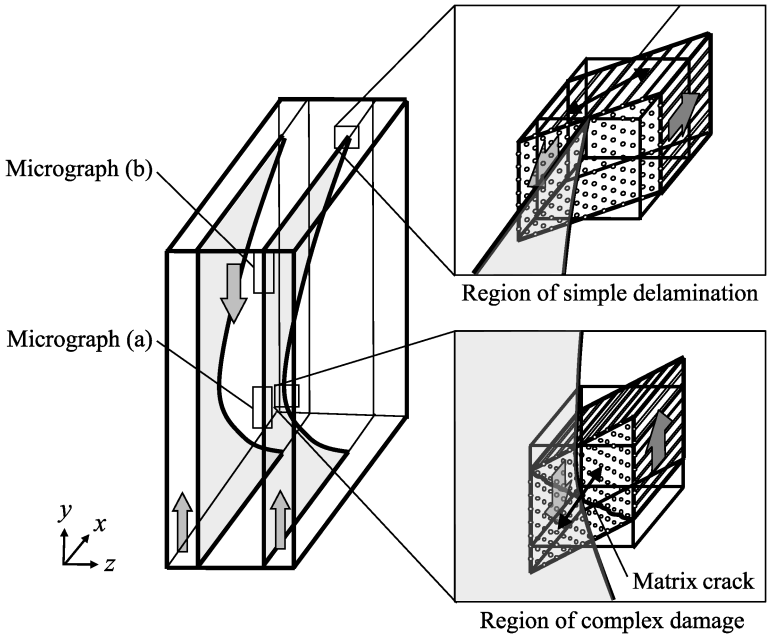

Figure 7. Fracture morphology depending on stress state and fiber orientation.

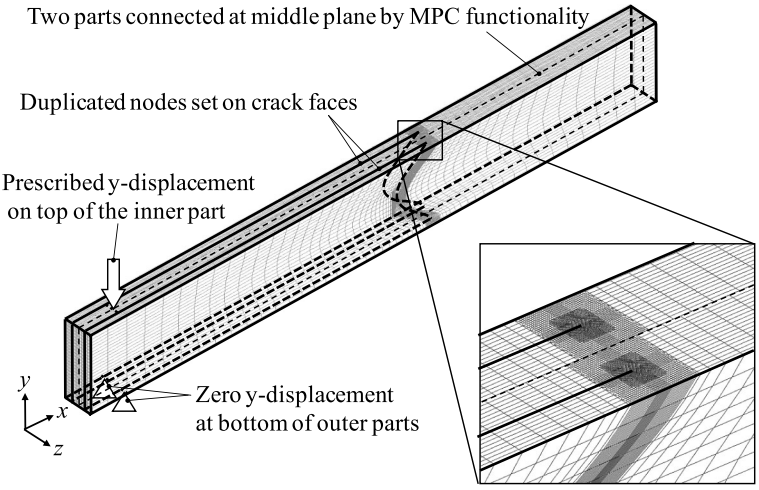

Figure 8. Finite element model and boundary conditions for energy release rate calculation.

a material constant because the occurrence of shear-induced matrix cracks depends on various factors, including the stress states and the stacking sequence.

Figure 8 shows the finite element model and the boundary conditions. VCCT was used for calculation of the energy release rate components. The material properties for the analyses are shown in Table 1. The delaminations were introduced by using

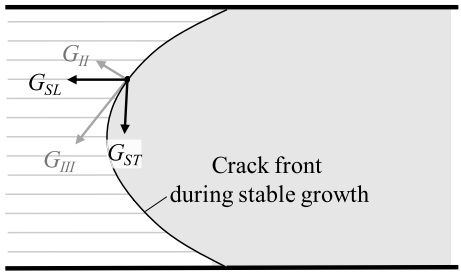

Figure 9. Mode decomposition of energy release rate.

duplicate nodes at the interfaces. Since the shapes of the two cracks were not the same, the whole specimen was modeled. Two half models were meshed independently based on the shapes of the crack fronts, expressed as spline curves, and the displacement continuity conditions were defined at the middle plane of the specimen by using the multi-point constraint (MPC) function. The supported lines on the bottom surfaces of the outer portions were fixed vertically and the prescribed displacement was applied at the loading line on the top surface of the center portion.

It was shown that the matrix cracks in the region in front of the delamination crack occurred primarily by the shear stress normal to the fiber, τ_{yz}. Thus, instead of G_{II} and G_{III}, the energy release rate was decomposed to components G_{ST} and G_{SL}, which were derived from the nodal forces and the relative displacements normal and parallel to the fiber, respectively. Figure 9 shows the decomposition of the shear components of the energy release rate.

The energy release rate distributions along the two crack fronts are plotted against the normalized vertical position in Fig. 10. Positions 0 and 1 represent the bottom and top of the specimen, respectively. The distributions at the three phases in Fig. 5 are plotted. At phase 1, the delamination propagated only near the edge of the crack front. The energy release rate was not sufficiently large to grow the delamination at the center portion. Because the length of crack 1 is smaller than that of crack 2, the overall energy release rate along crack 1 is higher. At phase 2, G_{ST} is very high in the middle of the crack front where the complex damage occurred and it is almost zero outside the complex damage area. The occurrence of the shear-induced matrix cracks is thought to be controlled by G_{ST}. It should be noted that $G_{\mathrm{Total}} = G_{\mathrm{II}} + G_{\mathrm{III}}$ in the simple delamination region remained virtually unchanged from phases 1–3.

3.2. Effect of Complex Damage on the Energy Release Rate Distribution

The finite element analyses described in the preceding section were performed without consideration of the existence of the shear-induced matrix cracks in the complex damage region. It was confirmed that the interlaminar fracture resistance in the simple delamination region was appropriately evaluated by the finite element analyses in Section 3.1 by performing additional finite element analyses with consideration of the existence of the matrix cracks.

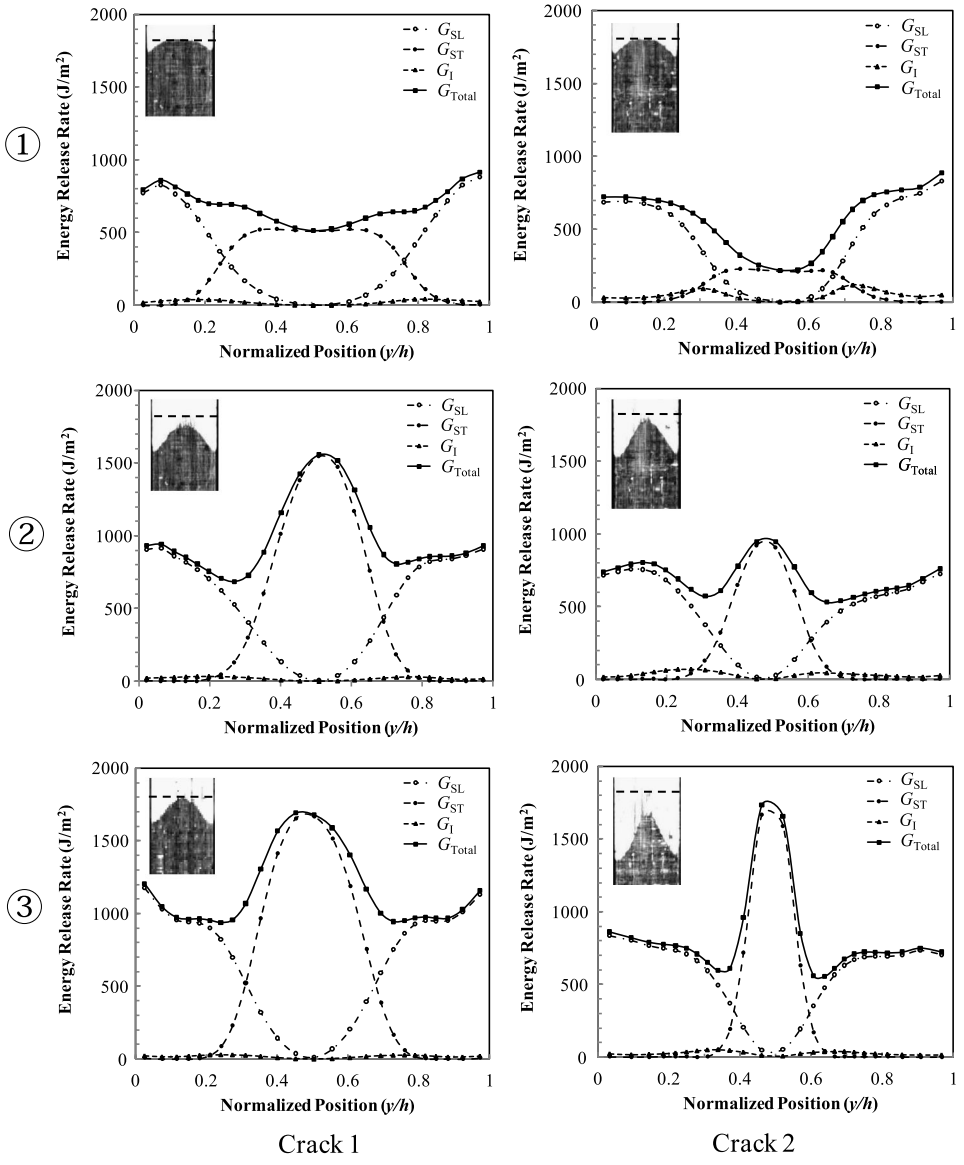

Figure 10. Energy release rate distributions.

The load transfer capability of the matrix in the complex damage region was degraded due to the existence of the matrix cracks. The effect of the degradation on the energy release rate distribution was examined. This kind of degradation is often expressed as the reduction of elastic constants in a finite element damage propagation analysis [24–26]. Therefore, elastic constants E_T and G_{TT} in the complex damage region were reduced to 1/2, 1/4 and 1/8 of the original values.

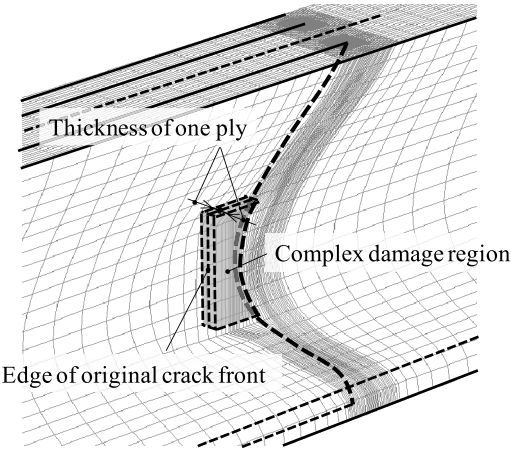

Figure 11. Region in finite element model representing stiffness degradation of complex damage region.

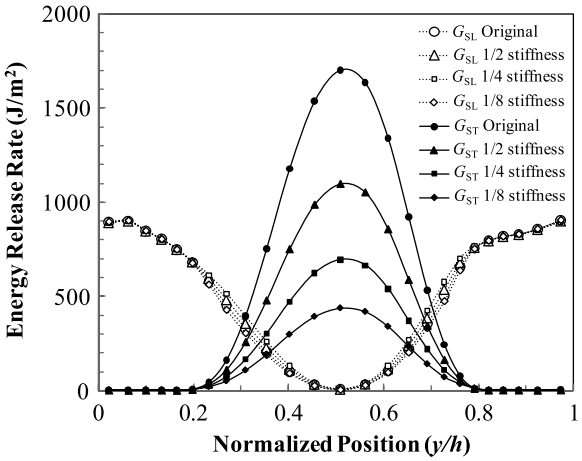

Figure 12. Variation of energy release rate distribution with respect to reduction of elastic constants of elements in complex damage region.

The complex damage region was located between the original crack front and the measured crack front, as shown in Fig. 11. Figure 12 shows the variation of the energy release rate with respect to the reduction of elastic constants. As the elastic constants were reduced, the G_{ST} component of the energy release rate in the complex damage region greatly decreased. However, the G_{SL} component in the simple delamination region varied little with the reduction of the elastic constants, and the difference between the values with and without the reduction of the elastic constants was less than 5% of the original value. Therefore, the degradation of the load transfer capability of the matrix in the complex damage region did not have a significant effect on the energy release rate distribution in the simple delamination regions.

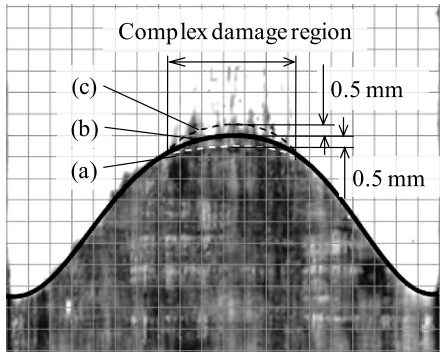

Figure 13. Shifted crack front curves in complex damage region.

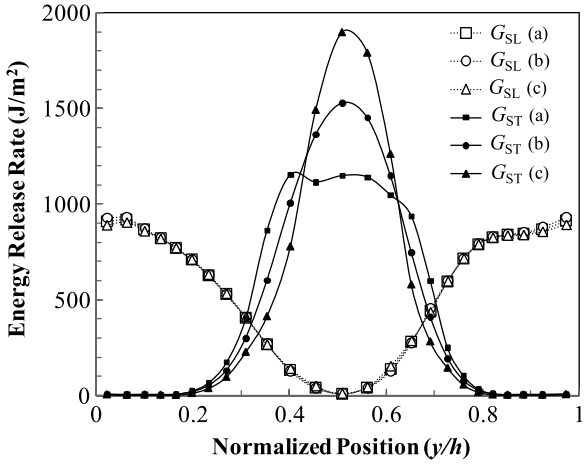

Figure 14. Change of energy release rate distribution with shift of approximated crack front curves.

The matrix cracks spread in front of and behind the delamination front. The complex damage region can be considered as a region of a wide process zone. Since the equivalent crack front should be located somewhere in the process zone, we examined the change of the energy release rate distribution by shifting the measured crack front forward and backward in the process zone. An ultrasonic C-Scan image of the specimen and the shifted crack front curves are shown in Fig. 13.

Curve (b) in the middle of the process zone was defined at the position of the visually identified crack front in the C-Scan image. The other two curves, (a) and (c), were defined at the same distance of 0.5 mm from the middle curve in the crack propagation direction. Most matrix cracks were found within the length of 0.5 mm from the visually identified crack front when the transverse cross-sections of the specimen were observed with the microscope. Figure 14 shows the change of the energy release rate distribution with the shift of the measured crack front curve. The effect of the shift was large on the G_{ST} components and small on the G_{SL} compo-

nents. The G_{ST} components of curves (a) and (c) were approximately 25% different from those of curve (b) at the center of the specimen. The distribution of the G_{SL} components of the three curves was almost unchanged. It should be noted that the average of the total energy release rate along the whole crack front changed less than 1% with the shifts.

The stiffness degradation and the shift of the equivalent crack front with consideration of the shear-induced matrix cracks in the complex damage region only slightly affected the distribution of the G_{SL} components of the energy release rate in the simple delamination region. In contrast, the stiffness degradation and the shift of the equivalent crack front greatly affected the distribution of the G_{ST} components in the complex damage region. Thus, the interlaminar fracture resistance in the simple delamination region can be evaluated from the G_{SL} components calculated with the finite element analysis described in Section 3.1.

3.3. Average Fracture Resistances in the Simple Delamination and Complex Damage Regions

The average fracture resistances in the simple delamination region and in the complex damage region were evaluated, respectively. The average fracture resistance in the simple delamination region, $\overline{R}_s$, was calculated using the following equation:

$$\overline{R}_s = \frac{1}{w_s} \int_{\Gamma s} G_{SL}(y)\, dy, \tag{1}$$

where Γ_s is the crack front of the simple delamination region and w_s is the total width of the simple delamination region in the transverse direction of the specimen. The average fracture resistance in the complex damage region, $\overline{R}_c$, was evaluated by

$$\overline{R}_c = \frac{1}{w_c}(\overline{R} \cdot 2h - \overline{R}_s \cdot w_s), \tag{2}$$

where $w_c = 2h - w_s$ is the total width of the complex damage region in the transverse direction of the specimen. $\overline{R}$ is the average fracture resistance of the specimen, which was obtained from the test results by the area method, and h is the height of the specimen. The results of the three specimens were averaged for each type of specimen.

The calculated fracture resistances in the regions of simple delamination and complex damage are shown in Fig. 15. The fracture resistance in the simple delamination region varies little with the specimen dimensions. The fracture resistances obtained in this study were slightly higher than that obtained by the ENF tests. This difference occurred because the initiation toughness of the unstable crack propagation was measured with the ENF tests but the toughness during the stable crack growth was measured with the DNSCB tests. The fracture resistance in the complex damage region was approximately 1.5–2 times higher than that in the simple delamination region. Therefore, the fracture morphology was found to strongly affect the fracture resistance of composite laminates.

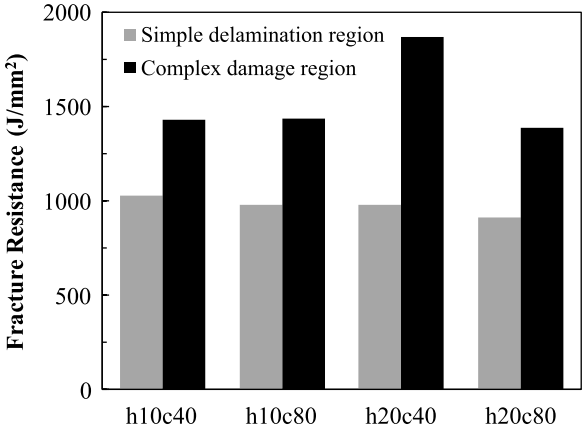

Figure 15. Fracture resistance in regions of simple delaminations and complex damage.

4. Conclusion

The fracture resistance of the interface of two 0° layers of composite laminates under the mixed-mode II and III crack propagation condition was studied using the DNSCB test method. The change in the fracture morphology and its effect on the fracture resistance were discussed through components G_{SL} and G_{ST} of the energy release rate. The components are based on the directions of the fiber at the interface. Complex damage consisting of delaminations and shear-induced matrix cracks distributed in the neighboring plies of the interface formed where G_{ST} was considerably high. However, the delaminations grew without the shear-induced matrix cracks where G_{ST} was almost zero. The fracture morphology strongly affected the fracture resistance. The fracture resistance in the region of complex damage was approximately 1.5–2 times higher than that in the region of simple delamination.

Acknowledgement

We acknowledge the support of the Japan Aerospace Exploration Agency.

References

1. J. M. Whitney, Stress analysis of the double cantilever beam specimen, *Compos. Sci. Technol.* **23**, 201–219 (1985).
2. P. Robinson and D. Q. Song, A modified DCB specimen for mode I testing of multidirectional laminates, *J. Compos. Mater.* **26**, 1554–1557 (1992).
3. A. B. de Morais, M. F. de Moura, A. T. Marques and P. T. de Castro, Mode I interlaminar fracture of carbon/epoxy cross-ply composites, *Compos. Sci. Technol.* **62**, 679–686 (2002).
4. L. A. Carlsson, J. W. Gillespie and R. B. Pipes, On the analysis and design of end notched flexure (ENF) specimen for measuring mode II fracture toughness, *Compos. Sci. Technol.* **20**, 594–604 (1986).
5. L. A. Carlsson, J. W. Gillespie and B. R. Trethewey, Mode II interlaminar fracture of graphite/epoxy and graphite/PEEK, *J. Reinforc. Plast. Compos.* **5**, 170–187 (1986).

6. F. Ozdil, L. A. Carlsson and P. Davies, Beam analysis of angle-ply laminate end-notched flexure specimens, *Compos. Sci. Technol.* **58**, 1929–1938 (1998).
7. J. R. Reeder and J. R. Crews, Mixed-mode bending method for delamination testing, *AIAA Journal* **28**, 1270–1276 (1990).
8. M. L. Benzeggagh and M. Kenane, Measurement of mixed-mode delamination fracture toughness of unidirectional glass/epoxy composites with mixed-mode bending apparatus, *Compos. Sci. Technol.* **56**, 439–449 (1996).
9. B. W. Kim and A. H. Mayer, Influence of fiber direction and mixed-mode ratio on delamination fracture toughness of carbon/epoxy laminates, *Compos. Sci. Technol.* **63**, 695–713 (2003).
10. N. Svensson and M. D. Gilchrist, Mixed-mode delamination of multidirectional carbon fiber/epoxy laminates, *Mech. Compos. Mater. Struct.* **5**, 291–307 (1998).
11. A. Sjogren and L. E. Asp, Effects of temperature on delamination growth in a carbon/epoxy composite under fatigue loading, *Intl J. Fatigue* **24**, 179–184 (2002).
12. E. S. Greenhalgh, C. R. Rogers and P. Robinson, Fractographic observations on delamination growth and the subsequent migration through the laminate, *Compos. Sci. Technol.* **69**, 2345–2351 (2009).
13. G. Becht and J. W. Gillespie, Design and analysis of crack rail shear specimen for mode III interlaminar fracture, *Compos. Sci. Technol.* **31**, 143–157 (1988).
14. S. L. Donaldson, Mode III interlaminar fracture characterization of composite materials, *Compos. Sci. Technol.* **32**, 225–249 (1988).
15. P. Robinson and D. Q. Song, The development of an improved mode III delamination test for composites, *Compos. Sci. Technol.* **52**, 217–233 (1994).
16. J. Li, S. M. Lee, E. W. Lee and T. K. O'Brien, Evaluation of the edge crack torsion (ECT) test for mode III interlaminar fracture toughness of laminated composites, *J. Compos. Technol. Res.* **19**, 174–183 (1997).
17. A. B. de Morais and A. B. Pereira, Mode III interlaminar fracture of carbon/epoxy laminates using a four-point bending plate test, *Compos. Part A* **40**, 1741–1746 (2009).
18. K. Trakas and M. T. Kortschot, The relationship between critical strain energy release rate and fracture mode in multidirectional carbon-fiber/epoxy laminates, in: *Compos. Mater.: Fatigue Fract.*, E. Armanios (Ed.), Vol. 6, pp. 283–304, *ASTM STP*, Vol. 1285, American Society for Testing and Materials, Philadelphia (1997).
19. X. Li, L. A. Carlsson and P. Davies, Influence of fiber volume fraction on mode III interlaminar fracture toughness of glass/epoxy composites, *Compos. Sci. Technol.* **64**, 1279–1286 (2004).
20. A. Szekrenyes, Delamination fracture analysis in the G_{II}–G_{III} plane using prestressed transparent composite beams, *Intl J. Solids Struct.* **44**, 3359–3378 (2007).
21. A. B. de Morais and A. B. Pereira, Mixed mode II + III interlaminar fracture of carbon/epoxy laminates, *Compos. Sci. Technol.* **68**, 2022–2027 (2008).
22. H. Suemasu, A. Kondo, K. Gozu and Y. Aoki, Novel test method for mixed mode II and III interlaminar fracture toughness, *Adv. Compos. Mater.* **19**, 349–361 (2010).
23. A. Kondo, Y. Sato, H. Suemasu, K. Gozu and Y. Aoki, Characterization of fracture resistance of carbon/epoxy composite laminates during mixed-mode II and III stable damage propagation, *J. Japan Soc. Compos. Mater.* **36**, 5 (2010).
24. S. C. Tan, A progressive failure model for composite laminates containing openings, *J. Compos. Mater.* **25**, 556–577 (1991).
25. P. P. Camanho and F. L. Mathews, A progressive damage model for mechanically fastened joints in composite laminates, *J. Compos. Mater.* **33**, 2248–2280 (1999).
26. A. C. Orifici, I. Herszberg and R. S. Thomson, Review of methodologies for composite material modelling incorporating failure, *Compos. Struct.* **86**, 194–210 (2008).